Bi modified oxidized tubular carbon nitride with high-yield singlet oxygen for propylparaben degradation: Implication for a novel oxygen activation mechanism

Yu-Wei Li [a,b], Shu-Zhi Li [a,b], Li-Yan Liu [a,b], Zi-Feng Zhang [a,b], Wan-Li Ma [a,b,*]

[a] *International Joint Research Center for Persistent Toxic Substances (IJRC-PTS), State Key Laboratory of Urban Water Resource and Environment, Harbin Institute of Technology, Harbin 150090, China*
[b] *Heilongjiang Provincial Key Laboratory of Polar Environment and Ecosystem (HPKL-PEE), Harbin 150090, China*

A B S T R A C T

The separation of electron-hole was the challenge in photocatalytic oxidation technology. In this study, Bi-OxTCN photocatalyst was prepared by introducing oxygen-containing functional groups and Bi metal into tubular g-C_3N_4 (TCN) to explore energy transfer mediated oxygen activation mechanism. Compared with TCN, the apparent rate constant of propylparaben (PrP) degradation on 0.8-Bi-OxTCN improved approximately 5.9 times. The installed Bi metal and oxygen-containing functional groups could improve spin-orbit coupling and narrow energy barrier between singlet and triplet state (decreasing from 0.310 eV to 0.168 eV), resulting in selective generation of high-yield singlet oxygen ($^1O_2$). The $^1O_2$ yield in 0.8-Bi-OxTCN was increased by 18 times in comparison with TCN. According to the density function theory calculations, the $^1O_2$ mainly attacked the benzene ring, hydroxyl and carboxyl group of PrP to form p-hydroxybenzoic acid, phenols, and benzoquinones. In summary, the study provides a novel oxygen activation pathway for photocatalytic oxidation technology in water treatment.

1. Introduction

Propylparaben (PrP) is widely used in medical products, personal care products, and food preservatives [1–3]. Therefore, PrP has been frequently detected in environmental water systems ranging from several ng L^{-1} to µg L^{-1} [4,5]. Furthermore, PrP has also been found in human tissue, blood, and breast milk, which suggested their occurrence in human beings [6,7]. As a potential emerging organic pollutant, it was found that PrP has acute and/or chronic toxicity to animals, even to human health [8–10]. Besides, PrP in water environment could generate several by-products [10,11]. Therefore, it is necessary to develop effective treatment technology to eliminate PrP in water. Recently, the photocatalytic oxidation process (PCOP) has attracted extensive attentions due to its stable redox ability, green and sustainable nature, and excellent renewability [11–13]. According to previous studies, the photocatalytic degradation of PrP was reported, which confirmed the application of PCOP for PrP removal. However, these reported PCOPs were still need to strictly control the reaction conditions (such as specific

pH values), and more deep discussion should be conducted for clarifying the transformation mechanism of PrP.

Graphitic carbon nitride (g-C_3N_4) is widely used in PCOP due to its environmentally benign property, high chemical stability, and tunable band gap [14–17]. However, the shortcomings of low specific surface area, high recombination rate of electron-hole pairs, limited active sites, and poor light absorbance dramatically restrict the practical application of g-C_3N_4. In order to solve the above problems, some synthesis strategies were proposed, such as nanomorphology control [18–20], heteroatom doping [21–24], surface sensitization [25], and heterojunction recombination [26–28]. All those modification methods are designed to produce more reactive oxygen species (ROSs), which is the prerequisite for g-C_3N_4 during PCOP.

In general, electron and energy transfer processes are the main generation pathways of ROS, and a simplified Jablonski diagram [29, 30] was made in Fig. 1 to understand the basic behaviors with g-C_3N_4 after light activation. Under light irradiation, electron in g-C_3N_4 is firstly excited from ground state (S_0) to singlet state (S_1) by charge transfer
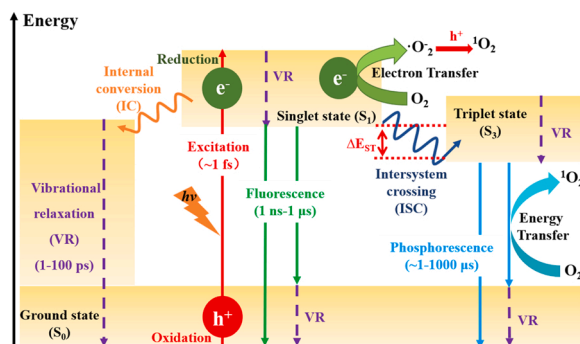
Fig. 1. Illustration of electron and energy transfer processes for $^1O_2$ generation in semiconductors after light activation.

process. The electron in S_1 could react with O_2 to form·O_2^- and $^1O_2$, thus, restraining electron-hole recombination (i.e. the electron return S_0 by emitting fluorescence) [12,31–33], which is a core problem in most current studies of g-C_3N_4. However, the powerful Coulomb interactions between electron and hole can hardly be conquered [34], and it is difficult to provide abundant energy disordered interfaces for exciton dissociation [35,36]. Recently, the energy transfer process has attracted more attentions and been applied to produce $^1O_2$ through transferring energy from triplet excitons to ground state oxygen, which was called energy transfer mediated O_2 activation pathway [37–39]. The electron could transfer from S_1 to lower-energy triplet state (S_3) through intersystem crossing (ISC) process [40], and the bound state system composed of electrons in S_3 and hole in S_0 is called triplet excitons, which could release phosphorescence. However, the photogenerated electrons in g-C_3N_4 are mostly singlet state, which limit the amount of triplet excitons, resulting in the low $^1O_2$ yield [37,41]. According to the first-order perturbation theory, the amount of triplet excitons can be influenced by spin-orbit coupling and energy barrier (ΔE_{ST}) between singlet state and triplet state of the matrix [39,42,43]. Therefore, enhancing spin-orbit coupling and narrowing ΔE_{ST} in g-C_3N_4 could favor triplet excitons generation, leading to high-yield $^1O_2$ generation. It was demonstrated that $^1O_2$ yield was highly correlated to oxygen-containing functional groups, such as carbonyl groups [38,39]. Furthermore, the introduction of heavy metal atom into catalyst to generate a unique coordinative structure could facilitate ISC process, which could increase the amount of triplet excitons by reducing ΔE_{ST}, and hence enhance the $^1O_2$ yield [44,45].

Based on the above mentioned successful experiences in previous studies, Bi modified oxidized tubular carbon nitride (Bi-OxTCN) with high yield of $^1O_2$ was prepared to explore the energy transfer mediated oxygen activation mechanism and apply for the PrP removal in this study. The objectives of this study were: 1) to synthesize Bi-OxTCN by incorporating Bi metal and oxygen-containing functional groups; 2) to investigate the structure and morphology of photocatalysts; 3) to explore the photocatalytic degradation performance of PrP by Bi-OxTCN; 4) to explore the generation mechanism of $^1O_2$; and 5) to clarify the role of $^1O_2$ on PrP degradation mechanism.

2. Experimental section

2.1. Photocatalysts synthesis methods

In this study, all the reagents were analytical grade, which can be found in details in Supporting Information (SI, Text S1).

Tubular g-C_3N_4 (TCN): The synthetic procedure of TCN was prepared according to previous studies with some modifications [19,46]. First, 3.5 g melamine was dissolved into 70 mL of deionized water under a water bath at 90 °C with strong stirring for 40 min. Subsequently, the above mixture was transferred into an autoclave with Teflon liner to

subject hydrothermal treatment at 180 °C for 24 h. After that, the obtained supramolecular intermediate was centrifuged, washed with deionized water for three times, and then dried in an oven at 60 °C for 12 h. Finally, the white powder was heated at 500 °C for 4 h with a ramp rate of 2 °C /min under nitrogen atmosphere.

Bi modified oxidized tubular g-C_3N_4 (Bi-OxTCN): The synthetic procedure of Bi-OxTCN was same as TCN, except for adding 1.0 mol/L H_2SO_4 as well as different amounts of Bi(NO$_3$)$_3$5 H_2O (0.2, 0.4, 0.6, 0.8, 1.0 mmol/L) into 70 mL deionized water during the procedure. The final products were defined as 0.2-Bi-OxTCN, 0.4-Bi-OxTCN, 0.6-Bi-OxTCN, 0.8-Bi-OxTCN, and 1-Bi-OxTCN in this study. According to the analysis by the Inductively Coupled Plasma-Optical Emission Spectrometer (ICP-OES, Optima 8300), the actual Bi content in the series of Bi-OxTCN products was determined to be 0.048, 0.33, 0.55, 0.74, and 1.0 wt%, respectively. As a comparison, the same synthetic procedure without adding Bi(NO$_3$)$_3$0.5 H_2O was prepared to obtain oxidized tubular g-C_3N_4, which was named as OxTCN in this study.

2.2. Characterization methods

The characterization methods of photocatalysts can be found in details in Text S2.

2.3. Photocatalytic activity experiment

For each degradation test, 20 mg of photocatalysts was added into 50 mL of PrP aqueous solution (10 ppm). A solar simulator equipped with a 70 W full spectrum metal halide lamp was used as light source of the photocatalytic oxidation system, which can emit light covering almost all wavelengths of sunlight (all visible light and some ultraviolet light). Prior to irradiation, the PrP solution with photocatalysts were stirred in dark for 1 h to achieve adsorption-desorption equilibrium. As shown in Fig. S1, the degradation of PrP was performed under a nearly pure photocatalytic condition with negligible adsorption and photolysis activities. During PCOP, 2.0 mL suspensions were sampled at intervals of 5 min, and filtered with a 0.2 μm polyvinylidene fluoride (PVDF) Whatman syringe filter. All the experiments were repeated for three times in order to obtain trustable results. The analytical methods of PrP and intermediates are provided in Text S3. In order to evaluate the stability of the photocatalysts, four cycling test experiments with PrP degradation were conducted in this study, which can be found in details in Text S4.

The removal efficiency (R, %) of PrP during PCOP was calculated by Eq. (1):

$$R = \frac{C_0 - C_t}{C_0} \times 100\%$$ (1)

where C_0 is the initial concentration of PrP; C_t is the measured concentration of PrP at time t.

The Pseudo-first order kinetic model was applied for fitting PrP degradation [21,47], and the corresponding apparent rate constant (k) was calculated by Eq. (2):

$$k = \frac{\ln(C_0/C_t)}{t}$$ (2)

2.4. Identification methods of active species

In this study, TMB was firstly applied to evaluate the molecular oxygen activation properties and identify the generated specific RSs (such as·OH,·O_2^-, $^1O_2$, H_2O_2 and h$^+$) [38,40,48]. In detail, 20 μL photocatalyst suspension (0.5 g/L) and 20 μL TMB solution (18 mM) were added to 2 mL acetate buffer solution (HAc/NaAc, pH = 4) [38]. Subsequently, the obtained solution was subjected to an UV–vis spectrophotometer at 380 nm to measure the TMB oxidation ability after light irradiation for 2, 4, 6, 8, and 10 min, respectively.

To better clarify the contribution of active species generated by 0.8-Bi-OxTCN during PCOP, a series of scavenging experiments were conducted in this study, which can be found in details in Text S5.

According to the method in a previous study [21], the contribution of each active species (R') on PrP degradation was calculated by Eq. (3):

$$R' \approx \frac{(k - k_i)}{k} \qquad (3)$$

where k_i is apparent rate constant of PrP degradation with quencher i.

2.5. Theoretical computation

As one of the useful theoretical tool, the density function theory (DFT) is widely applied in the field of quantum chemical calculation, which was also used for the theoretical computation in this study. In order to figure out the degradation pathway of PrP, the active sites of PrP molecules were analyzed by the Wiberg bond order, the lowest unoccupied molecular orbital (LUMO) – the highest occupied molecular (HOMO) frontal orbitals, and the Fukui function density (FFD) calculated by Gaussian 09 W [49] and Multiwfn 3.8 [50–52], respectively. Furthermore, the acute and chronic toxicities of PrP and its intermediates towards fish, daphnia and green algae were estimated based on the European Union Criteria (described in Annex VI of Directive 67/548/EEC) and the Chinese Hazard Evaluation Criteria for New Chemical Substances (HJ/T154–2004) [53,54], respectively. The specific calculation details can be found in Text S6.

3. Results and discussion

## 3.1. Structure, morphology and photoelectric properties

The structure and surface morphology of photocatalysts were observed by scanning electron microscopy (SEM) and transmission electron microscope (TEM). As shown in SEM images (Fig. 2a-c), all photocatalysts exhibited a similar rod-like tetragonal structure with a diameter of 1–3 μm, indicating that the acid treatment and introduction of Bi element did not significantly change the microstructure of TCN. According to previous studies [46,55,56], there were three main reactions for the formation of tubular structure during the hydrothermal process: the melamine partially turned into cyanuric acid at first, and then the rest of melamine combined with the generated cyanuric acid to form supramolecular intermediate through hydrogen bonding, finally the tubular g-C$_3$N$_4$ was obtained through thermal polymerization. The tubular structure could increase the specific surface area and offer more multiple light reflection/scattering channels [46], which could improve light absorption capacity, promote diffusion of reactant and product molecules, and expose more active edges, leading to the enhancement of photocatalytic performance. The TEM image (Fig. 2d) of 0.8-Bi-OxTCN further indicated that the tubular structure was successfully synthesized, and the wall of tube was composed of several layers. As shown in elemental mappings (Fig. 2e), C, N, O as well as Bi element were uniformly distributed on the surface of 0.8-Bi-OxTCN, indicating the successful introduction of Bi element and oxygen species. The high-resolution TEM image of 0.8-Bi-OxTCN is exhibited in Fig. 2f, and the 0.323 nm lattice spacing was observed, which could be
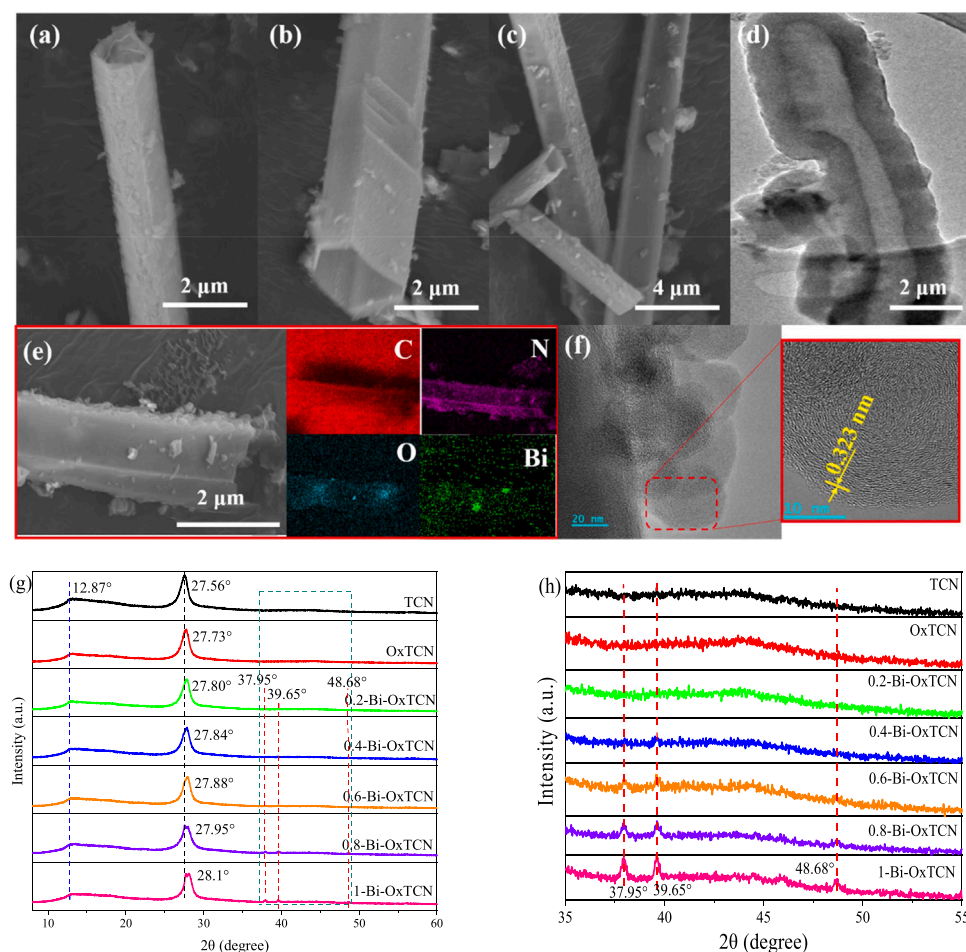
Fig. 2. SEM images of (a) TCN, (b) OxTCN, (c) 0.8-Bi-OxTCN. (d) TEM image, (e) Elemental mappings, and (f) HRTEM image of 0.8-Bi-OxTCN. (g) XRD patterns, and (h) magnified view of the three peaks at around 37.95°, 39.65° and 48.68° of TCN, OxTCN, and a series of Bi-OxTCN.

attributed to the (110) plane of the metal Bi (JCPDS # 44–1246) [57, 58]. The X-ray diffraction (XRD) patterns of TCN, OxTCN and a series of Bi-OxTCN are shown in Fig. 2g. Two typical peaks were observed at around 12.87° and 27.56° in all photocatalysts, corresponding to the (100) crystal plane of tris-s-triazine unit and the (002) plane diffraction formed by stacking of conjugated aromatic planes [59], respectively. Compared with TCN, the (100) diffraction peaks of OxTCN and a series

of Bi-OxTCN became weaker, meanwhile, the (002) peaks significantly shifted to high angle (from 27.56° to 28.10°), indicating that the crystallinity was decreased and the periodic structure was destroyed after acid treatment and introducing Bi element on TCN. Furthermore, three new diffraction peaks located at 37.95°, 39.65° and 48.68° were observed in the enlarged XRD patterns (Fig. 2h), corresponding to the (104), (110), and (202) diffraction peaks of Bi^0 based on the standard
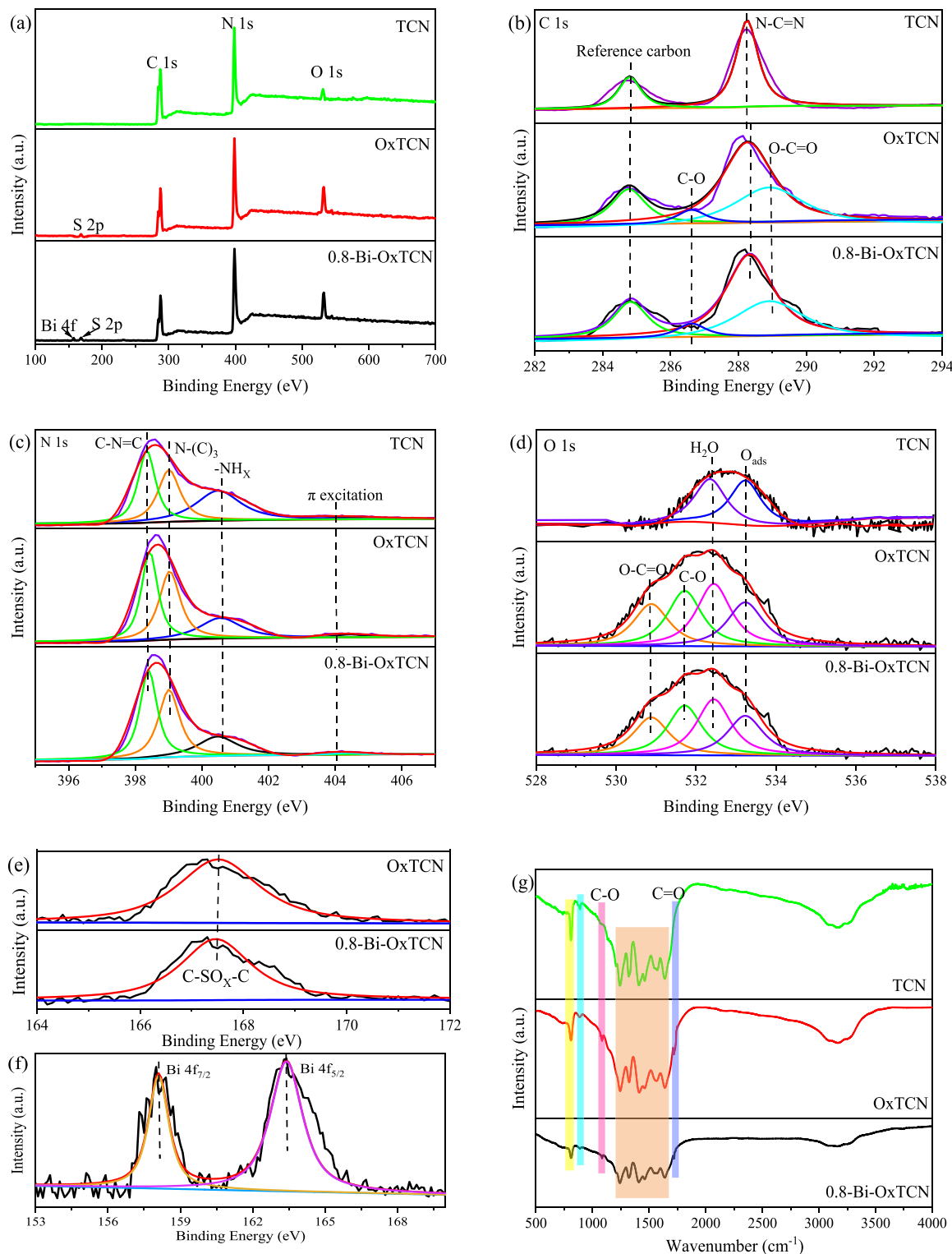
Fig. 3. XPS spectrum of TCN, OxTCN, and 0.8-Bi-OxTCN: (a) survey spectra, (b) C 1 s, (c) N 1 s, (d) O 1 s (e) S 2p of OxTCN, and 0.8-Bi-OxTCN. (f) Bi 4 f of 0.8-Bi-OxTCN. (g) FT-IR spectrum of TCN, OxTCN, and 0.8-Bi-OxTCN.

card of bismuth metal JCPDS NO. 05–0519 [57], respectively, which also suggested that Bi metal had been successfully assembled on the surface of TCN. In addition, the peak intensity of Bi metal increased gradually along with the increase of Bi content.

To characterize the types of introduced oxygen species and Bi metal, the X-ray photoelectron spectroscopy (XPS) was applied in this study. In the full XPS spectrum (Fig. 3a), 0.8-Bi-OxTCN consisted mainly of C, N, O, S, and Bi. Compared with TCN, the oxygen content of OxTCN and 0.8-Bi-OxTCN increased after acid treatment. For C 1 s spectrum (Fig. 3b), two peaks at 284.8 and 288.2 eV were observed in all photocatalysts, assigning to reference carbon [21] and N–C$=$N bonds [39], respectively, moreover, two new peaks on OxTCN and 0.8-Bi-OxTCN with binding energy located at 286.5 and 289.0 eV belonged to C–O and O–C$=$O bonds, respectively [38,41,60]. Furthermore, the peak of N–C$=$N bond was found to blueshift by about 0.1 eV, which might be caused by the weakened conjugation of tri-s-triazine structure and the covalent-bonding effect of oxygen-containing functional groups on g-C$_3$N$_4$ planes [39]. As displayed in Fig. 3c, four typical broad peaks were observed in all photocatalysts with binding energy of 398.4, 399.1, 400.8 and 404.0 eV, assigning to C–N$=$C, N–(C)$_3$, –NH$_X$, and the π-π * , respectively [38,61]. As displayed in O 1 s high-resolution spectra (Fig. 3d), the peaks at 532.4 eV and 533.3 eV were ascribed to H$_2$O and adsorbed O$_2$ (O$_{ads}$), respectively [38]. Compared with TCN, the new peaks at 530.7 eV and 531.6 eV confirmed the generation of O–C$=$O bond [62] and C–O bond [63] in OxTCN and 0.8-Bi-OxTCN, which implied that O atoms were directly introduced in the lattice of TCN after acid treatment. Moreover, the element analyses revealed that the introduced amount of O element was about 4.2% in mass (Table S1). As shown in Fig. 3e, the peak at 167.5 eV was assigned to C–SO$_x$–C bonds, indicating the oxysulfide superseded lattice nitrogen atoms in polymer matrix [64–66]. From Fig. S2, the isoelectric points of TCN, OxTCN, and 0.8-Bi-OxTCN were 3.7, 6.1, and 6.3, respectively. The increased isoelectric points of 0.8-Bi-OxTCN implied the formation of oxygen-containing functional groups in 0.8-Bi-OxTCN after acid treatment, which was consistent with a previous study [60]. As displayed in Fig. 3f, the high resolution XPS of Bi 4 f on 0.8-Bi-OxTCN presented two typical peaks with binding energies of 158.2 eV and 163.4 eV, corresponding to metallic Bi 4 f$_{7/2}$ and metallic Bi 4 f$_{5/2}$, respectively [57,67,68], which also indicated that Bi metal was successfully assembled on TCN. In summary, the oxygen-containing functional groups mainly included O–C$=$O, C–O and C–SO$_x$–C bond, and the element bismuth existed in the form of metal state in 0.8-Bi-OxTCN.

The direct evidence for the successful introduction of oxygen-containing functional groups was further confirmed by the Fourier Transform Infrared Spectroscopy (FT-IR), as shown in Fig. 3g. Compared with TCN, the peak of triazine unit (810.2 cm^{-1}) on OxTCN and 0.8-Bi-OxTCN became weaker, indicating that the original ordered structure was destroyed. The peak of isolated hydrogen and tensile C$=$N vibration conjugated aromatic rings at 889.8 and 1300–1700 cm^{-1} gradually weakened, which may be caused by the replacement of oxygen-containing functional groups after oxidation with H$_2$SO$_4$ [60,66]. It was worth noting that the OxTCN and 0.8-Bi-OxTCN exhibited two new peaks originating from the C–O and C$=$O bond at 1080 and 1720 cm^{-1}, which revealed the successful introduction of oxygen-containing functional groups on TCN by acid treatment [37,38].

The light-harvesting ability is an important parameter for the photocatalytic performance of photocatalysts, therefore, the UV–vis diffuse reflectance spectra (DRS) were measured in this study. As exhibited in Fig. S3, 0.8-Bi-OxTCN showed the highest visible light absorption capacity, indicating that the introduction of Bi metal and oxygen-containing functional groups could enhance the visible light absorption ability. Furthermore, the enhancement of visible light absorption could generate more photogenerated e$^-$-h$^+$ pairs, leading to the high photocatalytic activity.

3.2. Photocatalytic degradation performance

As shown in Fig. 4a, the removal efficiencies of PrP by TCN, OxTCN and 0.8-Bi-OxTCN were 47.2%, 60.1% and 99.0%, respectively, after 40 min under solar light irradiation, indicating that the improvement of photocatalytic activity was achieved through introducing oxygen-containing functional groups and Bi metal in TCN. With the increase of Bi content, the PrP removal efficiency firstly increased and then decreased, and 0.8-Bi-OxTCN exhibited the highest removal efficiency of PrP. The excessive Bi metal loaded on the surface of OxTCN would affect absorption of visible light or become new recombination centers by forming the nanoparticles or clusters [69]. The reaction kinetics curves of different photocatalysts are displayed in Fig. 4b. The *k* value of 0.8-Bi-OxTCN was the highest (*k* = 0.101 min^{-1}), which was about 5.9 times higher than that of TCN. Therefore, 0.8-Bi-OxTCN exhibited the best photocatalytic performance for PrP degradation among all photocatalysts.

The cycle experiment was performed to evaluate the stability of 0.8-Bi-OxTCN (Fig. 4c). The removal efficiency of PrP was decreased to a certain extent after four cycles experiment, however, the PrP removal efficiency was still higher than 80.0%. In order to further evaluate the chemical stability of 0.8-Bi-OxTCN, the fresh synthesized and used 0.8-Bi-OxTCN were characterized via XRD, XPS and FT-IR. As exhibited in Fig. S4, after four cycling experiments, 0.8-Bi-OxTCN still basically maintained the previous chemical structure and composition. Furthermore, the ICP-OES analysis showed that the content of Bi in solution after four cycling experiments was below detection limit, indicating that the Bi would not dissolve into the reaction system to cause secondary pollution. These results all indicated that 0.8-Bi-OxTCN had good chemical stability. The mineralization performance during PCOP of PrP by 0.8-Bi-OxTCN was evaluated by the total organic carbon (TOC). As shown in Fig. 4d, the TOC removal efficiency was achieved to 56.2% after solar light irradiation for 120 min, indicating that 0.8-Bi-OxTCN had a strong oxidation ability with a high efficient mineralization property.

3.3. Identification of active species

Since the photocatalytic oxidation performance was caused by the active species during PCOP, it is necessary to identify the generated active species through TMB oxidation on TCN, OxTCN and 0.8-Bi-OxTCN. As shown in Fig. 5a, all photocatalysts displayed a distinguishable TMB oxidation characteristic under different gas atmospheres (i.e. O$_2$, N$_2$ and air). The highest absorbance occurred under O$_2$ atmospheres, which implied that the oxygen played a major role in TMB oxidation. Furthermore, the 0.8-Bi-OxTCN had the highest absorbance, followed by OxTCN and TCN, which indicated that 0.8-Bi-OxTCN generated the highest number of radicals. It was worth noting that TMB was still slightly oxidized under N$_2$ atmospheres, which might be due to the presence of h$^+$ oxidation [38,39].

It was reported that the introduction of oxygen-containing functional groups on g-C$_3$N$_4$ could change the generation pathway from·O$_2^-$ to ^{1}O$_2$ [39,60]. In order to confirm the types of generated ROSs on TCN, OxTCN, and 0.8-Bi-OxTCN during TMB oxidation, the TBA, SOD, L-histidine, CAT, and KI were introduced to quench·OH,·O$_2^-$, ^{1}O$_2$, H$_2$O$_2$, and h$^+$, respectively [40,48,70–73]. As exhibited in Fig. 5b, the absorbance of OxTCN and 0.8-Bi-OxTCN dramatically reduced in the presence of L-histidine, which indicated that ^{1}O$_2$ was the primary generated ROS on OxTCN and 0.8-Bi-OxTCN. In contrast, the addition of SOD into the TCN reaction system significantly inhibited TMB oxidation, which indicated that the main generated ROS on TCN was·O$_2^-$. The findings indicated that the presence of oxygen-containing functional groups could remarkably affect the oxygen activation mechanism on TCN, leading to dramatically enhancement of ^{1}O$_2$ generation. Furthermore, the introduction of Bi metal could further promote ^{1}O$_2$ production.

As the most direct evidence to identify radicals, the electron spin
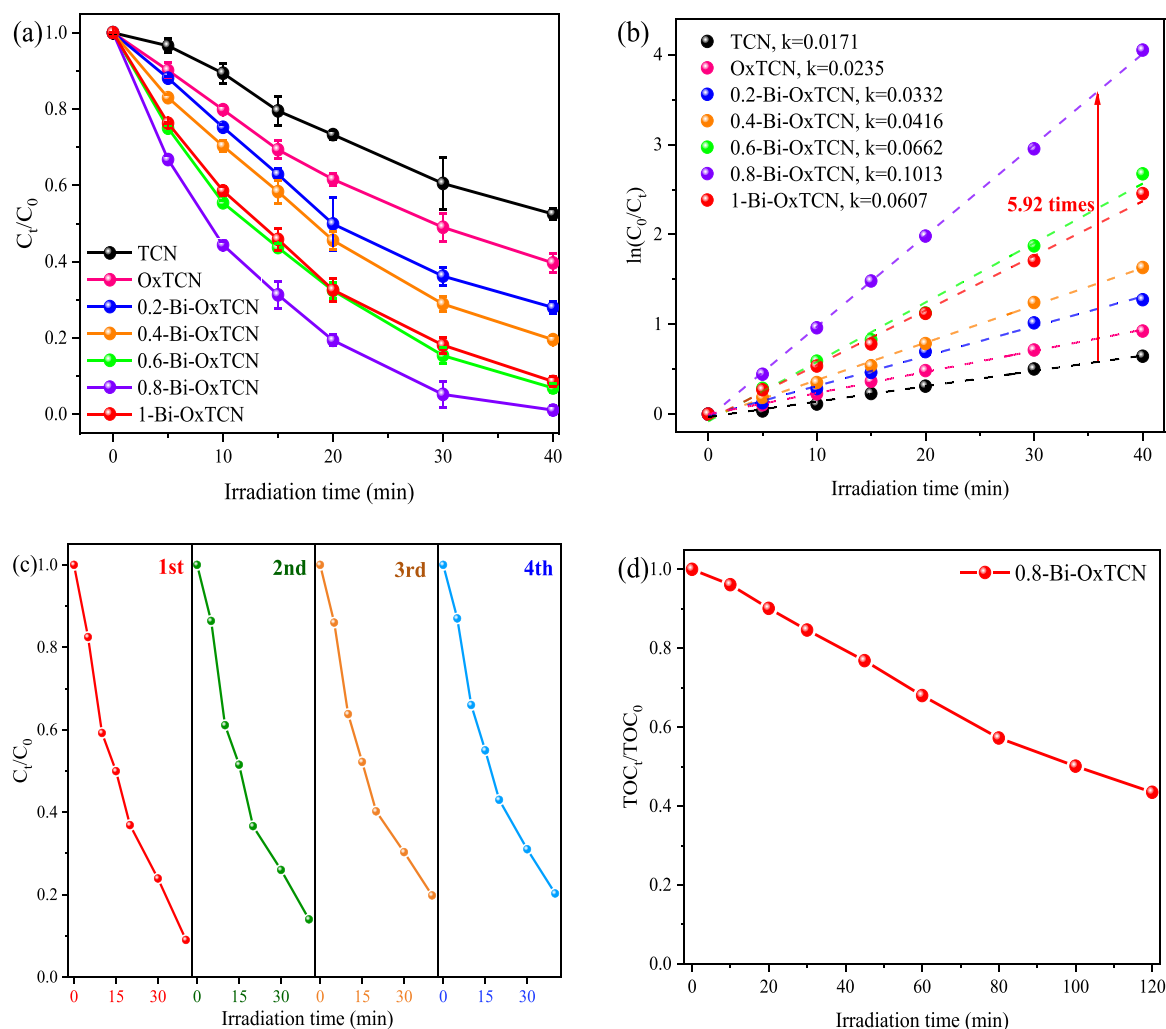
Fig. 4. (a) Removal efficiency and (b) corresponding kinetic curves under solar light irradiation on TCN, OxTCN and a series of Bi-OxTCN. (c) The cycling experiment of PrP degradation, and (d) TOC removal efficiency on 0.8-Bi-OxTCN.

resonance (ESR) test was also carried out in this study. Although·OH radicals did contribute a little to the TMB oxidation (Fig. 5b), no DMPO-·OH signal was observed in Fig. S5, which might be due to the low concentration of·OH radicals and/or the high detection limit of the EPR spectrometer. As shown in Fig. 5c, compared with TCN, OxTCN and 0.8-Bi-OxTCN showed relatively weaker DMPO-·O_2^- signal with intensity of 1:2:2:1, confirming that TCN could generate more·O_2^- rather than OxTCN and 0.8-Bi-OxTCN. From Fig. 5d, stronger TEMP-$^1O_2$ signal with intensity of 1:1:1 was observed on OxTCN and 0.8-Bi-OxTCN in comparison with TCN, indicating that OxTCN and 0.8-Bi-OxTCN could produce more $^1O_2$. Furthermore, the signal intensity of $^1O_2$ in 0.8-Bi-OxTCN (2.45 ×10^6) was increased by 0.7 times in comparison with OxTCN (1.41 ×10^6), implying that the introduction of Bi metal could further promote $^1O_2$ production. Based on the above analysis, the introduction of Bi metal and oxygen-containing functional groups into TCN could promote $^1O_2$ production.

To better clarify the contribution of each active species generated by 0.8-Bi-OxTCN during PCOP, a series of scavenging experiments were conducted with TBA, SOD, L-histidine, KI and HAD as the scavengers for·OH,·O_2^-, $^1O_2$, h$^+$ and triplet state, respectively [40,48,70–73]. Compared with other quenchers, the removal efficiency of PrP by 0.8-Bi-OxTCN decreased significantly from 94.7% to 42.7% after the quenching of $^1O_2$ by L-histidine (Fig. 5e). Fig. 5f exhibited the contribution of each active species and k values, which was estimated according to reaction kinetics of degradation (Fig. S6). Compared to no

quencher, the k value in the presence of L-histidine decreased 7.2 times. Since the radical chemistry is extremely complex during PCOP, the trapping agent also could affect the subsequent transformation processes between various active species, which would cause the total contribution of active species more than 100% [21]. Therefore, the contributions of active species were normalized. The contributions of·OH,·O_2^-, $^1O_2$, and h$^+$ were 5.80%, 27.2%, 41.9%, and 25.1%, respectively. Obviously, $^1O_2$ was the most important radical on 0.8-Bi-OxTCN, followed by·O_2^-, h$^+$ and·OH. According previous studies, radical oxidation pathway (·O_2^- and h$^+$) played primary role during PCOP on g-C_3N_4 [16,19,21]. Different from traditional radical oxidation pathway in g-C_3N_4, the non-radical dominated oxidation pathway caused by $^1O_2$ was proposed in the Bi-OxTCN system in this study.

3.4. Generation mechanism of singlet oxygen

In general, the $^1O_2$ is formed mainly through charge transfer or energy transfer [37,39,74]. There are two pathways to form $^1O_2$ by charge transfer: i)·O_2^- is oxidized by h$^+$, ii)·O_2^- is disproportionated [12,75,76]. Therefore,·O_2^- plays a decisive role in $^1O_2$ generation in charge transfer pathways. However, scavenging experiments in conjunction with ESR analysis indicated the limited amount of·O_2^- generated by OxTCN and 0.8-Bi-OxTCN. These findings implied that the $^1O_2$ generation was through energy transfer on OxTCN and 0.8-Bi-OxTCN. Energy transfer between singlet excitons and ground state of O_2 is spin forbidden,
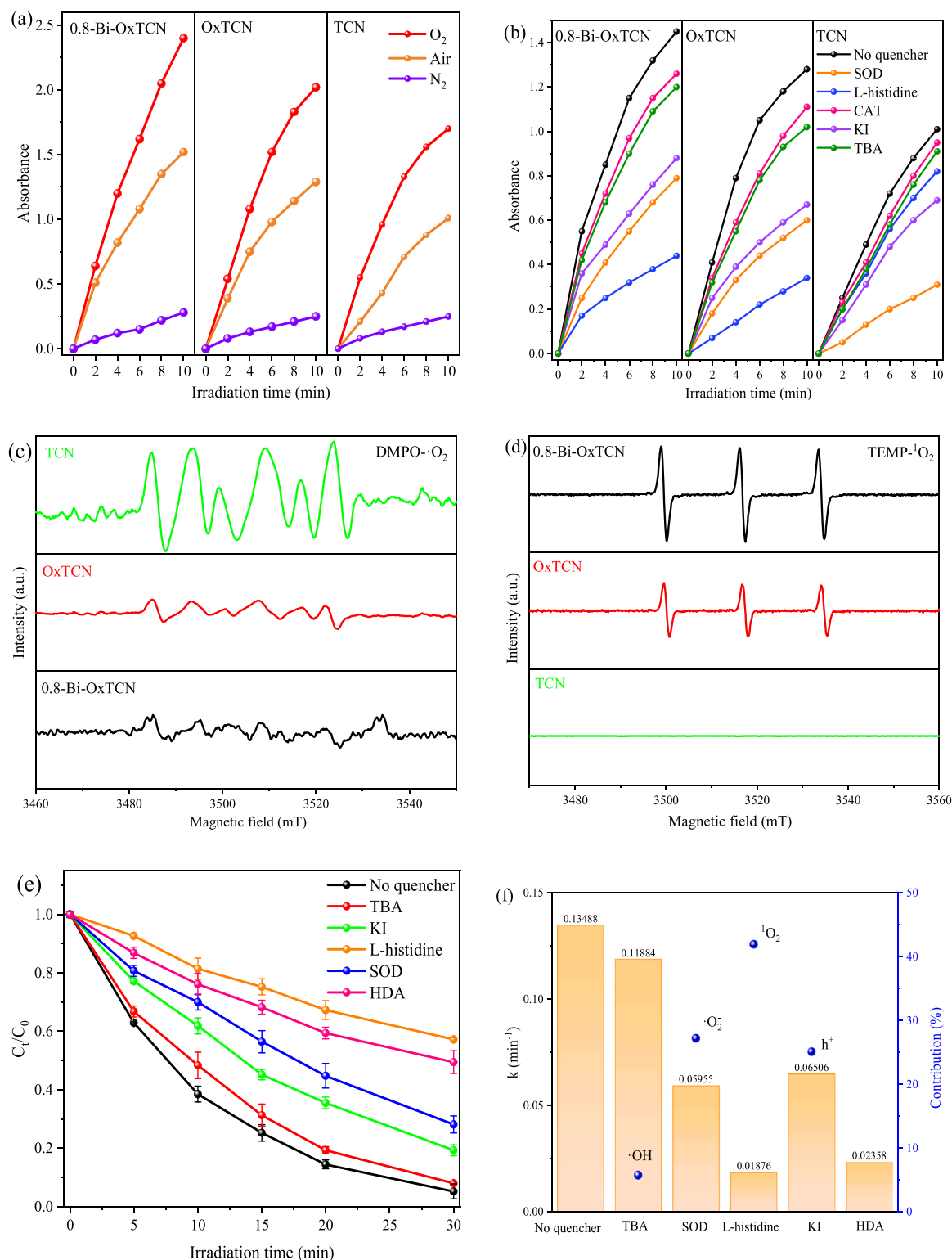
Fig. 5. (a) The absorbance change of TMB oxidation under different atmospheric conditions (air, N_2 and O_2), (b) the absorbance change of TMB oxidation in the presence of different quenchers on TCN, OxTCN and Bi-OxTCN. ESR spectra of TCN, OxTCN and Bi-OxTCN for (c) DMPO-·O_2^- adducts and (d) TEMP-$^1O_2$ adducts. (e) Photocatalytic degradation curves of PrP with different quenchers on 0.8-Bi-OxTCN. (f) The corresponding apparent rate constant as well as the relative contributions of different radicals.

therefore, the $^1O_2$ is mainly generated by energy transfer from triplet excitons to ground state of O_2 [38,39,76]. According to previous studies, the production pathway of $^1O_2$ through energy transfer was verified by the quencher (HDA) of triplet excitons [70,71]. As depicted in Figs. 5e and 5f, the PrP removal efficiency decreased significantly from 94.7% to

50.5% after adding HDA, and the corresponding *k* value decreased about 6.5 times in comparison with no quencher, which further confirmed that the energy transfer was the primary production pathway of $^1O_2$ in this study.

In order to better understand the role of Bi metal and oxygen-

containing functional groups on the formation of the $^1O_2$, the photo-luminescence measurements (including steady state fluorescence (PL), steady state phosphorescence (PH), and time resolved (TR)-PL and TR-PH) were carried out to further confirm the presence and intensity of $^1O_2$ on TCN, OxTCN and 0.8-Bi-OxTCN during PCOP. As displayed in Fig. 6a, compared with TCN, both OxTCN and 0.8-Bi-OxTCN exhibited a significantly reduced PL intensity, which did not suggest an improved

separation efficiency of electron-hole (e^--h^+) pairs, but a reduced singlet excitons production [18,38,75,77]. The behavior of photo-generated charge carrier was measured by electrochemical impedance spectroscopies (EIS) and transient photocurrent density to support the above conclusion. As shown in Fig. 6b, compared with TCN, OxTCN and 0.8-Bi-OxTCN had a much smaller radius, corresponding to a lower interface charge transfer resistance [75] and higher efficient separation
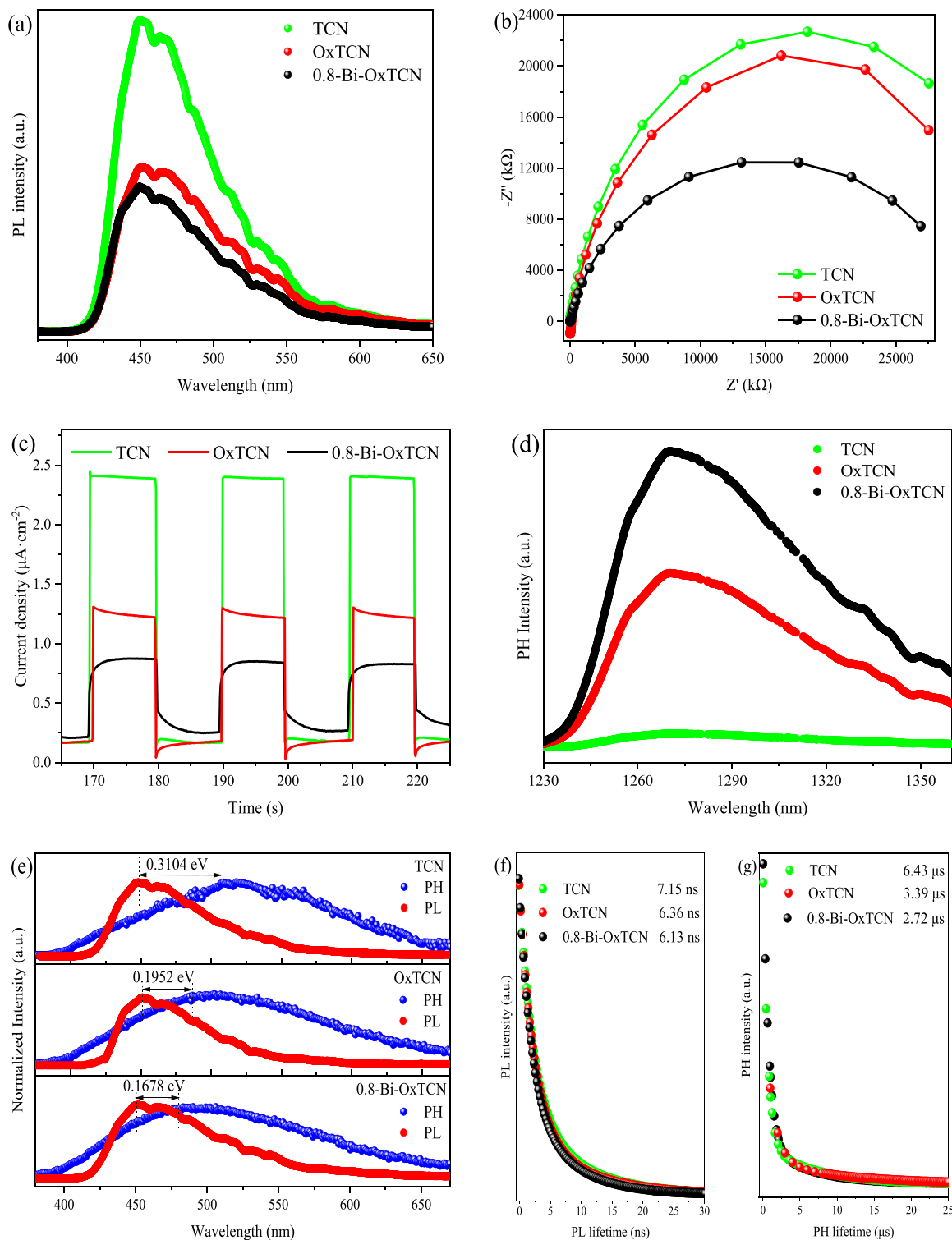
Fig. 6. (a) Steady state PL spectra, (b) EIS curves, (c) transient photocurrent curves, (d) near-infrared phosphorescence emission at 1270 nm of TCN, OxTCN and 0.8-Bi-OxTCN. (e) Normalized steady state PL and steady state PH spectra with excitation wavelength of 350 nm on TCN, OxTCN and 0.8-Bi-OxTCN. (f) TR-PL spectra and (g) TR-PH spectra of TCN, OxTCN and 0.8-Bi-OxTCN.

of e⁻-h⁺ pairs. Whereas, the values of current density of OxTCN and 0.8-Bi-OxTCN were obviously lower than that of TCN (Fig. 6c), implying that the recombination efficiency of e⁻-h⁺ pairs in OxTCN and 0.8-O-xTCN was higher than that of TCN. Therefore, it was speculated that ROS was formed through energy transfer mediated oxygen activation pathway in OxTCN and 0.8-Bi-OxTCN. The above hypothesis was further confirmed by the steady state PH spectra (Fig. S6), since the triplet excitons recombination could emit PH [38]. From Fig. S7, OxTCN and 0.8-Bi-OxTCN displayed much higher PH intensity than that of TCN, implying the enhancement of triplet excitons on OxTCN and 0.8-O-xTCN. The highest PH intensity and the lowest PL intensity on 0.8-Bi-O-xTCN confirmed that the most conversion of excitons from singlet state to triplet state, resulting in the $^1O_2$ generation in 0.8-Bi-OxTCN. Furthermore, the amount of $^1O_2$ is associated with PH intensity at 1270 nm [76], therefore, the near-infrared PH emission of TCN, OxTCN and 0.8-Bi-OxTCN was applied to measure the amount of $^1O_2$. As shown in Fig. 6d, the signal intensity of PH emission on 0.8-Bi-OxTCN was increased by 0.7 and 18 times in comparison with those of OxTCN and TCN, indicating that Bi atom and oxygen-containing functional groups greatly enhanced PH intensity by promoting the ISC process, resulting in the high $^1O_2$ yield in 0.8-Bi-OxTCN. Therefore, it can be concluded that the amount of $^1O_2$ in Bi-OxTCN system was increased by 18 times in comparison with that of TCN. Interestingly, a linear exponential relationship between the apparent rate constant of PrP degradation and the $^1O_2$ yield ($R^2 = 0.910$) was observed (Fig. S8), indicating that high $^1O_2$ yield could enhance the reaction rate of PrP degradation. The ΔE_{ST} values of OxTCN and 0.8-Bi-OxTCN were obtained by measuring the energy separation between PH and PL [78]. As shown in Fig. 6e, the ΔE_{ST} values of OxTCN and 0.8-Bi-OxTCN were 0.195 and 0.168 eV, respectively, which were more than 37% and 46% lower than that of TCN (0.310 eV). The reduced ΔE_{ST} values might improve the conversion from singlet state electron to triplet state electron by facilitating ISC process, resulting in $^1O_2$ production. According to the first-order perturbation theory, the introduction of Bi atom into OxTCN could generate a unique coordinative structure [44,45]. After incorporating Bi metal into OxTCN, the ΔE_{ST} of 0.8-Bi-OxTCN significantly reduced from 0.195 eV to 0.168 eV, which could further facilitate the conversion of electron from singlet state to triplet state through reducing ΔE_{ST} value. Subsequently, the triplet excitons could rapidly transfer the energy to adsorbed oxygen, leading to the generation of $^1O_2$.

To further support this claim, the kinetics of exciton transformation and $^1O_2$ generation were investigated by TR-PL and TR-PH. The average electron lifetimes (τ_{ave}) of photogenerated electrons produced by TCN, OxTCN and 0.8-Bi-OxTCN were calculated by Eq. (4):

$$\tau_{ave} = \frac{B_1\tau_1^2 + B_2\tau_2^2}{B_1\tau_1 + B_2\tau_2} \tag{4}$$

where, τ_1 and τ_2 respectively represent the two different lifetime components; B_1 and B_2 represent their corresponding normalized amplitudes [79].

The detailed information for these parameters is listed in Table S2, which were estimated from the Figs. 6f and 6g. As shown in Fig. 6f, a decrease PL lifetime was observed in OxTCN and 0.8-Bi-OxTCN in comparison with TCN, which might be ascribed to the acceleration of non-radiative ISC process [80]. This phenomenon also indicated more transformation from singlet exciton to triplet excitons during ISC process after introducing Bi metal and oxygen-containing functional groups. Furthermore, PL lifetime of OxTCN (6.36 ns) was higher than that of 0.8-Bi-OxTCN (6.13 ns), indicating that the introduction of Bi metal could further promote ISC process. Since the PH lifetime is closely related to the spin-flip conversion process of oxygen [39,81], TR-PH test was performed under air atmosphere. As shown in Fig. 6g, an apparent PH lifetime was reduced from 6.43 μs of TCN to 2.72 μs of 0.8-Bi-O-xTCN. The reduced PH lifetime was attributed to more energy transfer from triplet excitons to oxygen via spin-flip conversion, leading to more

$^1O_2$ production [80]. Furthermore, the PH lifetime of 0.8-Bi-OxTCN was shorter than that of OxTCN, indicating that the introduction of Bi metal could further promote $^1O_2$ production.

Therefore, a novel energy transfer mediated oxygen activation mechanism was proposed in 0.8-Bi-OxTCN. The incorporation of Bi atom and oxygen-containing functional groups (such as O–C=O, C–O and C–SOx–C bond) could promote spin-orbit coupling and decrease ΔE_{ST} between singlet and triplet state (from 0.310 eV in TCN to 0.168 eV in 0.8-Bi-OxTCN), which could facilitate the conversion from singlet to triplet state during ISC process. The $^1O_2$ was formed through the energy transfer from triplet excitons to ground state O_2 [38,39]. Furthermore, the strong spin-orbit coupling of Bi center could further reduce ΔE_{ST} to form more triplet excitons, leading to high yield of $^1O_2$ in Bi-OxTCN system.

3.5. Degradation pathway and ecotoxicity evaluation

In order to deeply figure out the degradation pathway of PrP by 0.8-Bi-OxTCN, the vulnerable active sites of PrP were predicted using DFT calculations [51]. Since $^1O_2$ was an electrophile [82] and a major ROS during PCOP, it was necessary to study the electrophilic reaction of $^1O_2$. It was reported that the electrophilic reaction was likely to occur when the energy difference between LUMO and HOMO ($\Delta E_{HOMO\text{-}LUMO}$) of molecule was less than 6.0 eV [37,83]. As shown in Table S3, the $\Delta E_{HOMO\text{-}LUMO}$ of PrP was 5.5 eV, therefore, the electrophilic reaction can occur during PCOP of PrP. The HOMO of PrP could be used to preliminarily predict the sites of electrophilic reaction based on the frontier electron density of HOMO [83], and the atoms with larger shadow implied the higher electronic energy and the smaller binding, leading to higher activity. As shown in Fig. 7a, the carboxyl group (O12 and O16), hydroxyl group (O24 and H25) and benzene ring (C1–C6) were more likely to be attacked by $^1O_2$. Furthermore, the electrophilic attack (f^-) of PrP was analyzed by Fukui function density (FFD), and the results are described in Table S4 and Fig. 7b. The atoms of PrP with larger green area and f^- value were easier to occur electrophilic attack by $^1O_2$ [84], thus, the O11 and O15 atoms and benzene ring were more vulnerable to be attacked by $^1O_2$. In general, a small value of Wiberg bond order implies low bond energy and easier cleavage [85]. As shown in Fig. 7c, the active chemical bonds of PrP were located at benzene ring, hydroxyl and carboxyl group. Therefore, it was speculated that the photocatalytic reaction of PrP was more likely occurred at benzene ring, hydroxyl and carboxyl group.

Based on the theoretical calculation and intermediates identification, the PrP degradation pathway was proposed in Fig. 7c. The detailed information of intermediates is displayed in Fig. S9 and Table S5. PrP was firstly degraded to form P1 (p-hydroxybenzoic acid) through the cleavage of the O–CH₂CH₂CH₃ bond under the simultaneous attack of·O_2^-, $^1O_2$ and h⁺ [52,54,86]. It was reported that monohydroxylation was the primary reaction pathway between $^1O_2$ and parabens [66, 87–89]. Accordingly, P1 could be further transformed to P2, P3 and P4 by the $^1O_2$ oxidation [54], which was named as the Pathway I. In Pathway II, the P5 and P6 were produced by successive decarbonylation and hydroxylation of P1 [54,86]. According to previous studies, $^1O_2$ could attack benzene ring of PrP to form hydroperoxides or endoperoxide intermediates [41,66], and then to generate benzoquinones by dehydration owing to its high electrophilicity [41,74]. Accordingly, the P5 and P6 were further oxidized by $^1O_2$ to form P7, P8 and P9, respectively.

Since radicals played an important role in photodegradation, thus, the mechanism and degradation products of PrP by different radicals were compared, and the results are shown in Table S6. The·OH was the primary ROS generated by TiO₂ through electron transfer mediated oxygen activation pathway, which mainly generated hydroxylated products on the aromatic ring or propyl ester chain [13]. In another study, it was found that the hydroxyl radical-induced degradation predominately attacked the alkyl chain of PrP by alkyl-H-abstraction route
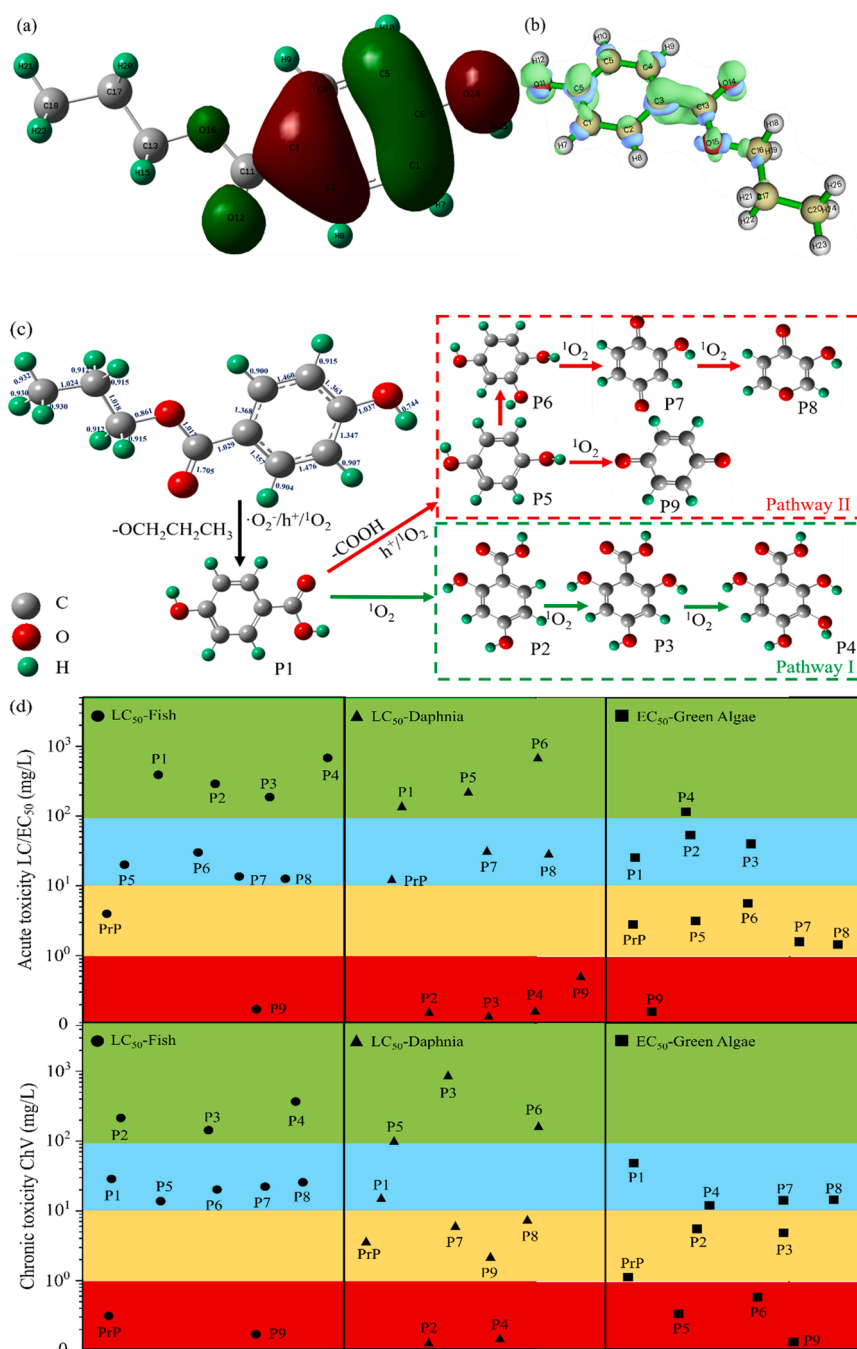
Fig. 7. (a) HOMO, (b) Fukui function density of PrP molecule. (c) The proposed degradation pathway of PrP with wiberg bond order. (d) Acute and chronic toxicity evaluation of PrP and its intermediates.

[53]. Different from the previous studies, $^1O_2$ was the main ROS in 0.8-Bi-OxTCN by the energy transfer mediated oxygen activation pathway, which attacked benzene ring, hydroxyl and carboxyl groups to form p-hydroxybenzoic acid, phenols and benzoquinones in this study.

The ecotoxicity (acute and chronic toxicity) evaluations of PrP and its intermediates towards fish, daphnia and green algae were estimated, the results are presented in Fig. 7d and Table S7. As shown in Fig. 7d, the red, purple, blue and green areas correspond to the level of very toxic, toxic, harmful and not harmful, respectively. Most of intermediates could be classified as "not harmful" or "harmful", however, the acute and chronic toxicities of P9 were higher than that of PrP. Furthermore, the P2 and P4 were not harmful to fish and green algae, but very toxic to daphnia, thus, the intermediates must be further mineralized by

delaying the photodegradation time to achieve green by-products.

4. Conclusion

In this study, the Bi-OxTCN photocatalyst was successfully synthesized and exhibited remarkable photocatalytic performance for PrP removal. According to characterization and experiment results, the Bi metal and oxygen-containing functional groups (including O–C═O, C–O and C–SO_x–C bond) were introduced into TCN. The $^1O_2$ played primary role in Bi-OxTCN during PrP photocatalytic degradation. Compared with TCN, the 0.8-Bi-OxTCN promoted spin-orbit coupling and decreased ΔE_{ST} value, which could facilitate the conversion of electrons from singlet state to triplet state during ISC process, leading to the high

selective $^1O_2$ production. Therefore, a novel energy transfer mediated photocatalytic oxygen activation mechanism was provided in 0.8-Bi-OxTCN system. Based on the proposed degradation pathway of PrP, the generated $^1O_2$ mainly attacked the electron-rich groups of PrP to form p-hydroxybenzoic acid, phenols, and benzoquinones. This study not only offers a feasible strategy to selectively form $^1O_2$ on g-C₃N₄, but also provides a new insight into the designing photocatalyst with high-efficient ROS production.

CRediT authorship contribution statement

Yu-Wei Li: Conceptualization, Methodology, Investigation, Writing – original draft. **Shu-Zhi Li:** Investigation, Writing – review & editing. **Li-Yan Liu:** Writing – review & editing. **Zi-Feng Zhang:** Writing – review & editing. **Wan-Li Ma:** Methodology, Investigation, Project administration, Funding acquisition, Writing – review & editing.

Declaration of Competing Interest

The authors declare that they have no known competing financial interests or personal relationships that could have appeared to influence the work reported in this paper.

Data availability

Data will be made available on request.

Acknowledgments

Appendix A. Supporting information

Supplementary data associated with this article can be found in the online version at doi:10.1016/j.apcatb.2022.122025.

References

[1] W.L. Ma, X. Zhao, Z.Y. Lin, M.O. Mohammed, Z.F. Zhang, L.Y. Liu, W.W. Song, Y. F. Li, A survey of parabens in commercial pharmaceuticals from China and its implications for human exposure, Environ. Int. 95 (2016) 30–35.

[2] J.M. Braun, A.C. Just, P.L. Williams, K.W. Smith, A.M. Calafat, R. Hauser, Personal care product use and urinary phthalate metabolite and paraben concentrations during pregnancy among women from a fertility clinic, J. Expo. Sci. Environ. Epidemiol. 24 (2014) 459–466.

[3] C. Haman, X. Dauchy, C. Rosin, J.-F. Munoz, Occurrence, fate and behavior of parabens in aquatic environments: a review, Water Res. 68 (2015) 1–11.

[4] W.L. Ma, X. Zhao, Z.F. Zhang, T.F. Xu, F.J. Zhu, Y.F. Li, Concentrations and fate of parabens and their metabolites in two typical wastewater treatment plants in northeastern China, Sci. Total Environ. 644 (2018) 754–761.

[5] V.H. Nguyen, L.A. Phan Thi, P.S. Chandana, H.T. Do, T.H. Pham, T. Lee, T. D. Nguyen, C. Le Phuoc, P.T. Huong, The degradation of paraben preservatives: recent progress and sustainable approaches toward photocatalysis, Chemosphere 276 (2021), 130163.

[6] M.J. Kim, C.H. Kim, M.J. An, J.H. Lee, G.S. Shin, J.Y. Hwang, J. Park, M. Song, H. Woo, Yh Kim, S. Rhee, J.W. Kim, Propylparaben induces apoptotic cell death in human placental BeWo cells via cell cycle arrest and enhanced caspase-3 activity, Mol. Cell. Toxicol. 16 (2020) 83–92.

[7] C.F. Grecco, I.D. Souza, M.E. Costa, Queiroz, Recent development of chromatographic methods to determine parabens in breast milk samples: a review, J. Chromatogr. B-Anal. Technol. Biomed. Life Sci. 1093 (2018) 82–90.

[8] M.L. Calma, P.M.B. Medina, Acute and chronic exposure of the holometabolous life cycle of Aedes aegypti L. to emerging contaminants naproxen and propylparaben, Environ. Pollut. 266 (2020), 115275.

[9] M.H. Chen, B. Yu, Z.F. Zhang, W.L. Ma, Occurrence of parabens in outdoor environments: implications for human exposure assessment, Environ. Pollut. 282 (2021), 117058.

[10] Y. Gao, T. An, H. Fang, Y. Ji, G. Li, Computational consideration on advanced oxidation degradation of phenolic preservative, methylparaben, in water: mechanisms, kinetics, and toxicity assessments, J. Hazard Mater. 278 (2014) 417–425.

[11] W. Wang, H. Wang, G. Li, P.K. Wong, T. An, Visible light activation of persulfate by magnetic hydrochar for bacterial inactivation: efficiency, recyclability and mechanisms, Water Res. 176 (2020), 115745.

[12] Y.W. Li, W.L. Ma, Photocatalytic oxidation technology for indoor air pollutants elimination: a review, Chemosphere 280 (2021), 130667.

[13] H. Fang, Y. Gao, G. Li, J. An, P.-K. Wong, H. Fu, S. Yao, X. Nie, T. An, Advanced oxidation kinetics and mechanism of preservative propylparaben degradation in aqueous suspension of TiO2 and risk assessment of its degradation products, Environ. Sci. Technol. 47 (2013) 2704–2712.

[14] Y. Li, M. Gu, T. Shi, W. Cui, X. Zhang, F. Dong, J. Cheng, J. Fan, K. Lv, Carbon vacancy in C3N4 nanotube: electronic structure, photocatalysis mechanism and highly enhanced activity, Appl. Catal. B: Environ. 262 (2020), 118281.

[15] X. Zheng, Q. Zhang, T. Chen, Y. Wu, J. Hao, C. Tan, P. Chen, F. Wang, H. Liu, W. Lv, G. Liu, A novel synthetic carbon and oxygen doped stalactite-like g-C3N4 for broad-spectrum-driven indometacin degradation, J. Hazard. Mater. 386 (2020), 121961.

[16] Y. Li, M. Gu, X. Zhang, J. Fan, K. Lv, S.A.C. Carabineiro, F. Dong, 2D g-C3N4 for advancement of photo-generated carrier dynamics: status and challenges, Mater. Today 41 (2020) 270–303.

[17] Q. Zhang, J. Chen, X. Gao, H. Che, P. Wang, Y. Ao, In-depth insight into the mechanism on photocatalytic synergistic removal of antibiotics and Cr (VI): the decisive effect of antibiotic molecular structure, Appl. Catal. B-Environ. 313 (2022), 121443.

[18] Z. Zeng, X. Quan, H. Yu, S. Chen, S. Zhang, Nanoscale lightning rod effect in 3D carbon nitride nanoneedle: Enhanced charge collection and separation for efficient photocatalysis, J. Catal. 375 (2019) 361–370.

[19] S. Wan, M. Ou, Q. Zhong, W. Cai, Haloid acid induced carbon nitride semiconductors for enhanced photocatalytic H2 evolution and reduction of CO₂ under visible light, Carbon 138 (2018) 465–474.

[20] K. Li, M. Zhang, X. Ou, R. Li, Q. Li, J. Fan, K. Lv, Strategies for the Fabrication of 2D Carbon Nitride Nanosheets, Acta Phys. -Chim. Sin. 37 (2021) 2008010.

[21] C. Zhang, D. Qin, Y. Zhou, F. Qin, H. Wang, W. Wang, Y. Yang, G. Zeng, Dual optimization approach to Mo single atom dispersed g-C3N4 photocatalyst: morphology and defect evolution, Appl. Catal. B: Environ. 303 (2022), 120904.

[22] Z. Mo, X. Zhu, Z. Jiang, Y. Song, D. Liu, H. Li, X. Yang, Y. She, Y. Lei, S. Yuan, H. Li, L. Song, Q. Yan, H. Xu, Porous nitrogen-rich g-C3N4 nanotubes for efficient photocatalytic CO₂ reduction, Appl. Catal. B: Environ. 256 (2019), 117854.

[23] X. Li, Z. Hu, Q. Li, M. Lei, J. Fan, S.A.C. Carabineiro, Y. Liu, K. Lv, Three in one: atomically dispersed Na boosting the photoreactivity of carbon nitride towards NO oxidation, Chem. Commun. 56 (2020) 14195–14198.

[24] W. Liu, P. Wang, J. Chen, X. Gao, H.N. Che, B. Liu, Y. Ao, Unraveling the mechanism on ultrahigh efficiency photocatalytic h2o2 generation for dual-heteroatom incorporated polymeric carbon nitride, Adv. Funct. Mater. (2022) 2205119.

[25] K. Saravanakumar, R. Karthik, S.M. Chen, J.V. Kumar, K. Prakash, V. Muthuraj, Construction of novel Pd/CeO2/g-C3N4 nanocomposites as efficient visible-light photocatalysts for hexavalent chromium detoxification, J. Colloid Interface Sci. 504 (2017) 514–526.

[26] Y. Li, F. Liu, M. Li, W. Li, X. Qi, M. Xue, Y. Wang, F. Han, Study on adsorption coupling photodegradation on hierarchical nanostructured g-C3N4/TiO2/activated carbon fiber composites for toluene removal, J. Sol. -Gel Sci. Technol. 93 (2019) 402–418.

[27] G. Li, X. Nie, J. Chen, Q. Jiang, T. An, P.K. Wong, H. Zhang, H. Zhao, H. Yamashita, Enhanced visible-light-driven photocatalytic inactivation of Escherichia coli using g-C3N4/TiO2 hybrid photocatalyst synthesized using a hydrothermal-calcination approach, Water Res. 86 (2015) 17–24.

[28] H. Che, X. Gao, J. Chen, J. Hou, Y. Ao, P. Wang, Iodide-induced fragmentation of polymerized hydrophilic carbon nitride for high-performance quasi-homogeneous photocatalytic H2O2 production, Angew. Chem. -Int. Ed. 60 (2021) 25546–25550.

[29] C. Chen, H. Ou, R. Liu, D. Ding, Regulating the photophysical property of organic/ polymer optical agents for promoted cancer phototheranostics, Adv. Mater. 32 (2020) 1806331.

[30] G. Feng, G.-Q. Zhang, D. Ding, Design of superior phototheranostic agents guided by Jablonski diagrams, Chem. Soc. Rev. 49 (2020) 8179–8234.

[31] Z. Hu, Z. Shen, J.C. Yu, Converting carbohydrates to carbon-based photocatalysts for environmental treatment, Environ. Sci. Technol. 51 (2017) 7076–7083.

[32] Y. Li, M. Gu, M. Zhang, X. Zhang, K. Lv, Y. Liu, W. Ho, F. Dong, C3N4 with engineered three coordinated (N3C) nitrogen vacancy boosts the production of 1O2 for Efficient and stable NO photo-oxidation, Chem. Eng. J. 389 (2020), 124421.

[33] Y. Li, M. Gu, T. Shi, W. Cui, X. Zhang, F. Dong, J. Cheng, J. Fan, K. Lv, Carbon vacancy in C3N4 nanotube: electronic structure, photocatalysis mechanism and highly enhanced activity, Appl. Catal. B-Environ. 262 (2020), 118281.

[34] J.C. Blancon, H. Tsai, W. Nie, C.C. Stoumpos, L. Pedesseau, C. Katan, M. Kepenekian, C.M.M. Soe, K. Appavoo, M.Y. Sfeir, S. Tretiak, P.M. Ajayan, M. G. Kanatzidis, J. Even, J.J. Crochet, A.D. Mohite, Perovskite physics extremely efficient internal exciton dissociation through edge states in layered 2D perovskites, Science 355 (2017) 1288–1291.

[35] Z.A. Lan, G. Zhang, X. Chen, Y. Zhang, K.A.I. Zhang, X. Wang, Reducing the exciton binding energy of donor-acceptor-based conjugated polymers to promote charge-induced reactions, Angew. Chem. -Int. Ed. 58 (2019) 10236–10240.

[36] L. Shi, C.K. Lee, A.P. Willard, The enhancement of interfacial exciton dissociation by energetic disorder is a nonequilibrium effect, Acs Cent. Sci. 3 (2017) 1262–1270.

[37] J. Brame, M. Long, Q. Li, P. Alvarez, Trading oxidation power for efficiency: differential inhibition of photo-generated hydroxyl radicals versus singlet oxygen, Water Res. 60 (2014) 259–266.

[38] Z. Zeng, Y. Fan, X. Quan, H. Yu, S. Chen, S. Zhang, Energy-transfer-mediated oxygen activation in carbonyl functionalized carbon nitride nanosheets for high-efficient photocatalytic water disinfection and organic pollutants degradation, Water Res. 177 (2020), 115798.

[39] H. Wang, S. Jiang, S. Chen, D. Li, X. Zhang, W. Shao, X. Sun, J. Xie, Z. Zhao, Q. Zhang, Y. Tian, Y. Xie, Enhanced singlet oxygen generation in oxidized graphitic carbon nitride for organic synthesis, Adv. Mater. 28 (2016) 6940–6945.

[40] Y.-Z. Chen, Z.U. Wang, H. Wang, J. Lu, S.-H. Yu, H.-L. Jiang, Singlet oxygen-engaged selective photo-oxidation over Pt nanocrystals/porphyrinic MOF: the roles of photothermal effect and Pt electronic state, J. Am. Chem. Soc. 139 (2017) 2035–2044.

[41] Y. Zhou, J. Jiang, Y. Gao, S.Y. Pang, Y. Yang, J. Ma, J. Gu, J. Li, Z. Wang, L. H. Wang, L.P. Yuan, Y. Yang, Activation of peroxymonosulfate by phenols: Important role of quinone intermediates and involvement of singlet oxygen, Water Res. 125 (2017) 209–218.

[42] T. van Westen, J. Gross, Accurate first-order perturbation theory for fluids: uf-theory, J. Chem. Phys. 154 (2021), 041102.

[43] C.A. Masmanidis, H.H. Jaffe, R.L. Ellis, Spin-orbit coupling in organic molecules, J. Phys. Chem. 79 (1975) 2052–2061.

[44] X. Liao, F. Wang, Y. Wang, W. Wei, Z. Xiao, H. Liu, Q. Hao, S. Lu, Z. Li, Functionalized g-C3N4 sheets assisted synthesis of growth-oriented MIL-88B-Fe with rod-like structure: Upgrading framework photo-catalytic performance and stability, Appl. Surf. Sci. 503 (2020), 144089.

[45] X. Jiang, S. Liu, W. Wang, S. Shi, Z. Zeng, C. Chen, Enhanced singlet oxygen generation in PCN-224-Zn without the need of electron-hole separation for efficient photocatalytic water disinfection, Appl. Surf. Sci. 575 (2022), 151769.

[46] Z. Mo, H. Xu, Z. Chen, X. She, Y. Song, J. Wu, P. Yan, L. Xu, Y. Lei, S. Yuan, H. Li, Self-assembled synthesis of defect-engineered graphitic carbon nitride nanotubes for efficient conversion of solar energy, Appl. Catal. B: Environ. 225 (2018) 154–161.

[47] H. Yang, T. An, G. Li, W. Song, W.J. Cooper, H. Luo, X. Guo, Photocatalytic degradation kinetics and mechanism of environmental pharmaceuticals in aqueous suspension of TiO2: a case of beta-blockers, J. Hazard. Mater. 179 (2010) 834–839.

[48] X. Sun, X. Luo, X. Zhang, J. Xie, S. Jin, H. Wang, X. Zheng, X. Wu, Y. Xie, Enhanced superoxide generation on defective surfaces for selective photooxidation, J. Am. Chem. Soc. 141 (2019) 3797–3801.

[49] Y. Gao, G. Li, Y. Qin, Y. Ji, B. Mai, T. An, New theoretical insight into indirect photochemical transformation of fragrance nitro-musks: Mechanisms, eco-toxicity and health effects, Environ. Int. 129 (2019) 68–75.

[50] T. Lu, F. Chen, Multiwfn: a multifunctional wavefunction analyzer, J. Comput. Chem. 33 (2012) 580–592.

[51] T. An, H. Yang, G. Li, W. Song, W.J. Cooper, X. Nie, Kinetics and mechanism of advanced oxidation processes (AOPs) in degradation of ciprofloxacin in water, Appl. Catal. B: Environ. 94 (2010) 288–294.

[52] T. An, L. Sun, G. Li, Y. Gao, G. Ying, Photocatalytic degradation and detoxification of o-chloroaniline in the gas phase: Mechanistic consideration and mutagenicity assessment of its decomposed gaseous intermediate mixture, Appl. Catal. B-Environ. 102 (2011) 140–146.

[53] Y. Gao, Y. Ji, G. Li, T. An, Theoretical investigation on the kinetics and mechanisms of hydroxyl radical-induced transformation of parabens and its consequences for toxicity: Influence of alkyl-chain length, Water Res. 91 (2016) 77–85.

[54] Y. Gao, X. Niu, Y. Qin, T. Guo, Y. Ji, G. Li, T. An, Unexpected culprit of increased estrogenic effects: Oligomers in the photodegradation of preservative ethylparaben in water, Water Res. 176 (2020), 115745.

[55] L. Chen, X. Zhao, X. Duan, J. Zhang, Z. Ao, P. Li, S. Wang, Y. Wang, S. Cheng, H. Zhao, F. He, P. Dong, C. Zhao, S. Wang, H. Sun, Graphitic carbon nitride microtubes for efficient photocatalytic overall water splitting: the morphology derived electrical field enhancement, ACS Sustain. Chem. Eng. 8 (2020) 14386–14396.

[56] S. Guo, Y. Tang, Y. Xie, C. Tian, Q. Feng, W. Zhou, B. Jiang, P-doped tubular g-C3N4 with surface carbon defects: universal synthesis and enhanced visible-light photocatalytic hydrogen production, Appl. Catal. B: Environ. 218 (2017) 664–671.

[57] Y. Yang, Z. Bian, L. Zhang, H. Wang, Bi@BiOx(OH)y modified oxidized g-C3N4 photocatalytic removal of tetracycline hydrochloride with highly effective oxygen activation, J. Hazard. Mater. 427 (2022), 127866.

[58] Z. Zhang, M. Chi, G.M. Veith, P. Zhang, D.A. Lutterman, J. Rosenthal, S. H. Overbury, S. Dai, H. Zhu, Rational Design of Bi Nanoparticles for Efficient Electrochemical CO2 Reduction: The Elucidation of Size and Surface Condition Effects, ACS Catal. 6 (2016) 6255–6264.

[59] J. Fu, Q. Xu, J. Low, C. Jiang, J. Yu, Ultrathin 2D/2D WO3/g-C3N4 step-scheme H2-production photocatalyst, Appl. Catal. B: Environ. 243 (2019) 556–565.

[60] Y. Yang, Z. Bian, Oxygen doping through oxidation causes the main active substance in g-C3N4 photocatalysis to change from holes to singlet oxygen, Sci. Total Environ. 753 (2021) 141908.

[61] K. Chu, Qq Li, Yp Liu, J. Wang, Yh Cheng, Filling the nitrogen vacancies with sulphur dopants in graphitic C3N4 for efficient and robust electrocatalytic nitrogen reduction, Appl. Catal. B-Environ. 267 (2020), 118693.

[62] J. Tian, L. Zhang, M. Wang, X. Jin, Y. Zhou, J. Liu, J. Shi, Remarkably enhanced H2 evolution activity of oxidized graphitic carbon nitride by an extremely facile K2CO3-activation approach, Appl. Catal. B-Environ. 232 (2018) 322–329.

[63] L. Yang, J. Huang, L. Shi, L. Cao, Q. Yu, Y. Jie, J. Fei, H. Ouyang, J. Ye, A surface modification resultant thermally oxidized porous g-C3N4 with enhanced photocatalytic hydrogen production, Appl. Catal. B: Environ. 204 (2017) 335–345.

[64] L. Jiang, X. Yuan, G. Zeng, X. Chen, Z. Wu, J. Liang, J. Zhang, H. Wang, H. Wang, Phosphorus and sulfur-codoped g-C3N4: Facile preparation, mechanism insight, and application as efficient photocatalyst for tetracycline and methyl orange degradation under visible light irradiation, ACS Sustain. Chem. Eng. 5 (2017) 5831–5841.

[65] H. Tang, Z. Xia, R. Chen, Q. Liu, T. Zhou, Oxygen doped g-C3N4 with nitrogen vacancy for enhanced photocatalytic hydrogen evolution, Chem. - Asian J. 15 (2020) 3456–3461.

[66] P. Sun, H. Liu, M. Feng, L. Guo, Z. Zhai, Y. Fang, X. Zhang, V.K. Sharma, Nitrogen-sulfur co-doped industrial graphene as an efficient peroxymonosulfate activator: Singlet oxygen-dominated catalytic degradation of organic contaminants, Appl. Catal. B: Environ. 251 (2019) 335–345.

[67] Y. Li, K. Lv, W. Ho, Z. Zhao, Y. Huang, Enhanced visible-light photo-oxidation of nitric oxide using bismuth-coupled graphitic carbon nitride composite heterostructures, Chin. J. Catal. 38 (2017) 321–329.

[68] R. Li, X. Ou, L. Zhang, Z. Qi, X. Wu, C. Lu, J. Fan, K. Lv, Photocatalytic oxidation of NO on reduction type semiconductor photocatalysts: effect of metallic Bi on CdS nanorods, Chem. Commun. 57 (2021) 10067–10070.

[69] Z. Zeng, Y. Su, X. Quan, W. Choi, G. Zhang, N. Liu, B. Kim, S. Chen, H. Yu, S. Zhang, Single-atom platinum confined by the interlayer nanospace of carbon nitride for efficient photocatalytic hydrogen evolution, Nano Energy 69 (2020), 104409.

[70] K.J. Moor, M. Schmitt, P.R. Erickson, K. McNeill, Sorbic acid as a triplet probe: triplet energy and reactivity with triplet-state dissolved organic matter via O-1(2) phosphorescence, Environ. Sci. Technol. 53 (2019) 8078–8086.

[71] M. Schmitt, K.J. Moor, P.R. Erickson, K. McNeill, Sorbic acid as a triplet probe: reactivity of oxidizing triplets in dissolved organic matter by direct observation of aromatic amine oxidation, Environ. Sci. Technol. 53 (2019) 8087–8096.

[72] Z. Hu, Z. Shen, J.C. Yu, Converting carbohydrates to carbon-based photocatalysts for environmental treatment, Environ. Sci. Technol. 51 (2017) 7076–7083.

[73] J. Lim, H. Kim, P.J.J. Alvarez, J. Lee, W. Choi, Visible light sensitized production of hydroxyl radicals using fullerol as an electron-transfer mediator, Environ. Sci. Technol. 50 (2016) 10545–10553.

[74] M.C. DeRosa, R.J. Crutchley, Photosensitized singlet oxygen and its applications, Coord. Chem. Rev. 233–234 (2002) 351–371.

[75] W. Zhang, W. Huang, J. Jin, Y. Gan, S. Zhang, Oxygen-vacancy-mediated energy transfer for singlet oxygen generation by diketone-anchored MIL-125, Appl. Catal. B: Environ. 292 (2021), 120197.

[76] Y. Nosaka, A.Y. Nosaka, Generation and detection of reactive oxygen species in photocatalysis, Chem. Rev. 117 (2017) 11302–11336.

[77] G. Zhang, G. Li, Z.A. Lan, L. Lin, A. Savateev, T. Heil, S. Zafeiratos, X. Wang, M. Antonietti, Optimizing optical absorption, exciton dissociation, and charge transfer of a polymeric carbon nitride with ultrahigh solar hydrogen production activity, Angew. Chem. -Int. Ed. 56 (2017) 13445–13449.

[78] D. Beljonne, Z. Shuai, G. Pourtois, J.L. Bredas, Spin-orbit coupling and intersystem crossing in conjugated polymers: a configuration interaction description, J. Phys. Chem. A 105 (2001) 3899–3907.

[79] H. Chauhan, Y. Kumar, J. Dana, B. Satpati, H.N. Ghosh, S. Deka, Photoinduced ultrafast charge separation in colloidal 2-dimensional CdSe/CdS-Au hybrid nanoplatelets and corresponding application in photocatalysis, Nanoscale 8 (2016) 15802–15812.

[80] W. Wu, C. Han, Q. Zhang, Q. Zhang, Z. Li, D.J. Gosztola, G.P. Wiederrecht, M. Wu, Functionalizing carbon nitride with heavy atom-free spin converters for enhanced 1O2 generation, J. Catal. 361 (2018) 222–229.

[81] C. Masmanidis, H. Jaffe, R. Ellis, Spin-orbit coupling in organic molecules, J. Phys. Chem. 79 (1975) 2052–2061.

[82] M. Zenzo, H. Shin`ya, A semiempirical molecular orbital study on the reaction of an aminopyrazolinyl azo dye with singlet molecular oxygen, Dyes Pigments 41 (1999) 1–10.

[83] K. Wojciechowski, L. Szuster, Photofading of derivatives of paraben (PHB) by AM1 and PM3 methods: a theoretical study, Comput. Chem. 7 (2019) 39–50.

[84] S. Le, C. Zhu, Y. Cao, P. Wang, Q. Liu, H. Zhou, C. Chen, S. Wang, X. Duan, V2O5 nanodot-decorated laminar C3N4 for sustainable photodegradation of amoxicillin under solar light, Appl. Catal. B: Environ. 303 (2022), 120903.

[85] Y. Wang, P. Yan, X. Dou, C. Liu, Y. Zhang, Z. Song, Z. Chen, B. Xu, F. Qi, Degradation of benzophenone-4 by peroxymonosulfate activated with microwave synthesized well-distributed CuBi2O4 microspheres: Theoretical calculation of degradation mechanism, Appl. Catal. B: Environ. 290 (2021), 120048.

[86] X. Zhang, Y. Liu, M. Ren, G. Yang, L. Qin, J. Guo, J. Meng, Precise carbon doping regulation of porous graphitic carbon nitride nanosheets enables elevated photocatalytic oxidation performance towards emerging organic pollutants, Chem. Eng. J. 433 (2022), 134551.

[87] D. Gryglik, M. Gmurek, The photosensitized oxidation of mixture of parabens in aqueous solution, Environ. Sci. Pollut. Res. 25 (2018) 3009–3019.

[88] M. Gmurek, M. Bizukojć, J. Mosinger, S. Ledakowicz, Application of photoactive electrospun nanofiber materials with immobilized meso-tetraphenylporphyrin for parabens photodegradation, Catal. Today 240 (2015) 160–167.

[89] M. Hu, J. Zhu, W. Zhou, Synthesis of oxygen vacancy-enriched N/P co-doped CoFe2O4 for high-efficient degradation of organic pollutant: mechanistic insight into radical and nonradical evolution, Environ. Pollut. 270 (2021), 116092.